Front. Phys. 13(4), 137304 (2018)
https://doi.org/10.1007/s11467-018-0770-6

RESEARCH ARTICLE

Spin-dependent transport properties and Seebeck effects for a crossed graphene superlattice *p-n* junction with armchair edge

Ben-Hu Zhou[1,†], Ben-Liang Zhou[2], Yang-Su Zeng[1], Man-Yi Duan[3], Guang-Hui Zhou[2,‡]

[1] *Department of Physics, Shaoyang University, Shaoyang 422001, China*
[2] *Department of Physics and Key Laboratory for Low-Dimensional Structures and Quantum Manipulation (Ministry of Education), Hunan Normal University, Changsha 410081, China*
[3] *College of Physics and Electronic Engineering, Sichuan Normal University, Chengdu 610068, China*
Corresponding authors. E-mail: †zhoubenhu@163.com, ‡ghzhou@hunnu.edu.cn
Received January 10, 2018; accepted February 5, 2018

Using the nonequilibrium Green's function method combined with the tight-binding Hamiltonian, we theoretically investigate the spin-dependent transmission probability and spin Seebeck coefficient of a crossed armchair-edge graphene nanoribbon (AGNR) superlattice *p-n* junction under a perpendicular magnetic field with a ferromagnetic insulator, where junction widths W_1 of 40 and 41 are considered to exemplify the effect of semiconducting and metallic AGNRs, respectively. A pristine AGNR system is metallic when the transverse layer $m = 3j + 2$ with a positive integer j and an insulator otherwise. When stubs are present, a semiconducting AGNR junction with width $W_1 = 40$ always shows metallic behavior regardless of the potential drop magnitude, magnetization strength, stub length, and perpendicular magnetic field strength. However, metallic or semiconducting behavior can be obtained from a metallic AGNR junction with $W_1 = 41$ by adjusting these physical parameters. Furthermore, a metal-to-semiconductor transition can be obtained for both superlattice *p-n* junctions by adjusting the number of periods of the superlattice. In addition, the spin-dependent Seebeck coefficient and spin Seebeck coefficient of the two systems are of the same order of magnitude owing to the appearance of a transmission gap, and the maximum absolute value of the spin Seebeck coefficient reaches 370 μV/K when the optimized parameters are used. The calculated results offer new possibilities for designing electronic or heat-spintronic nanodevices based on the graphene superlattice *p-n* junction.

Keywords crossed graphene superlattice *p-n* junction, spin-dependent transport properties, Seebeck coefficient, nonequilibrium Green's function

PACS numbers 73.22.-f, 73.63.-b, 72.25.Dc, 79.10.-n

1 Introduction

The Seebeck effect converts heat to electricity when a temperature difference exists between two ends of a junction, and thus has been used to harvest waste heat in industrial processes [1–3]. In the early days, the Seebeck effect was neglected because it is difficult to measure experimentally. Thanks to the development of microfabrication technology and low-temperature measurement technology, the Seebeck effect has been widely observed and experimentally studied in many systems, including semimetallic materials [4], superconductive materials [5], and carbon nanotubes [6]. The Seebeck coefficient (thermopower) of pristine graphene nanoribbons (GNRs) was experimentally measured recently, and the value of the Seebeck coefficient can reach ∼80 μV/K at room temperature [7–9]. A giant Seebeck coefficient (30 mV/K) has been theoretically predicted for graphene gated by a sequence of metal leads [10]. Ouyang and Guo [11] and Xing *et al.* [12] have calculated that the Seebeck coefficient of a GNR is two orders of magnitude larger than that of two-dimensional graphene. Further, the spin-dependent Seebeck effects in graphene and its

nanoribbons have also attracted attention. For example, a remarkable magneto-Seebeck effect has been predicted for zigzag graphene nanoribbon (ZGNR)-based spin valves and ZGNR heterostructures [13–16], and the spin-dependent Seebeck coefficient in ZGNRs can be enhanced by nitrogen-nitrogen or boron-nitrogen doping [17]. Chen and collaborators have predicted that the spin Seebeck coefficient S_S can reach 3.4 mV/K in GNRs with sawtooth zigzag edges owing to the large spin gap of sawtooth GNRs [18].

It is already well known that quantum confinement can lead to considerable enhancement of the Seebeck coefficient in nanoscale structures owing to resonant tunneling of electrons [19–23]. Thus, the thermoelectric properties of GNR junctions with various shapes have also been considered. For example, Xie *et al.* [24] have predicted that the Seebeck coefficient of a T-shaped GNR junction can be greatly enhanced by the quantum confinement effect of stub structure. Mazzamuto *et al.* [25] have found that a high Seebeck coefficient can be obtained for an S- or H-shaped GNR junction by alternating armchair and zigzag sections with different widths owing to resonant tunneling of electrons between these sections. Tran *et al.* [26] have predicted that a large Seebeck coefficient, $S > 2$ mV/K, and figure of merit, $ZT > 0.8$, can be achieved for a crossed superlattice armchair ribbon consisting of alternating graphene and boron nitride sections owing to the opening of a significant conduction energy gap and strong reduction of the phonon thermal conductance. A first-principle calculation has shown that a ZT value as high as ∼5 can be obtained by adjusting the gate voltages for a ZGNR-polyacene-ZGNR junction [27]. Additionally, structural defects, such as antidots, may also be a promising way to enhance the thermoelectric efficiency of GNRs. The thermoelectric properties of GNRs with antidot arrays have been theoretically studied, and high charge Seebeck coefficients have been achieved [28–31]. It has also been predicted that extremely high spin Seebeck coefficients can be obtained for a ZGNR with periodic antidot defects [32]. In the present work, we investigate primarily the effect of geometric structures on the thermoelectric properties of GNRs and attempt to improve the thermoelectric efficiency of GNRs by modulating the stub structures.

On the other hand, the graphene p-n junction has attracted much attention because it is a promising building block for future graphene electronics. The graphene p-n junction can be created experimentally by varying the gate voltage [33–36] or doping the underlying substrate.[37] Further, the p-n-p junction has also been realized experimentally [38, 39]. Motivated by these experimental findings, a large number of theoretical works have investigated the electrical transport in graphene p-n junctions and superlattices [40–48]. For example, several interesting transport phenomena are predicted for graphene p-n junctions owing to the massless Dirac nature of the carriers, including Klein tunneling [41], Veselago lensing [42], and scalable quantum resistance standards [43]. In addition, by varying the gate voltage, the charge carrier in graphene can be tuned from electronlike to holelike, and vice versa. Therefore, a graphene p-n junction can be a good candidate for studying the interplay between the electronlike and holelike quasiparticles. However, most previous works on graphene p-n junctions focused on their electrical transport properties. Investigation of the thermoelectric effect in such systems is sparsely reported, especially for a graphene crossed superlattice p-n junction. Although we have addressed this issue for a graphene crossed superlattice p-n junction with a zigzag edge [49], in this paper we extend our study to an armchair-edge graphene nanoribbon (AGNR) system.

In this paper, we present a comprehensive investigation of the spin-dependent transport and spin-related thermoelectric properties of a crossed AGNR-based superlattice p-n junction under a ferromagnetic (FM) insulator. AGNR superlattice p-n junctions with widths W_1 of 40 and 41 are considered. By using the nonequilibrium Green's function (NEGF) method combined with the tight-binding Hamiltonian [50–52], the spin dependence of the transmission probability and the dependence of the spin-related Seebeck coefficient on the potential drop, magnetization, number of periods of the superlattice, stub width, and magnetic field strength are calculated. It is found that the spin-dependent transmission probability and spin Seebeck coefficient for a crossed AGNR superlattice p-n junction can be controlled by varying the widths and geometric structure of the nanoribbons. It is well known that pristine AGNRs having a transverse layer $m = 3j + 2$ with a positive integer j are metallic, and otherwise they are semiconducting. In the presence of stubs, a semiconducting AGNR junction with width $W_1 = 40$ always shows metallic behavior regardless of the potential drop magnitude, magnetization strength, stub length, and perpendicular magnetic field strength. However, a metallic AGNR junction with width $W_1 = 41$ can present metallic or semiconducting behavior depending on the physical parameters mentioned above. Furthermore, a metal-to-semiconductor transition can be obtained for two systems by adjusting the number of periods of the superlattice. In addition, the spin-dependent Seebeck coefficient and spin Seebeck coefficient for crossed superlattice p-n junctions with widths $W_1 = 40$ and 41 are of the same order of magnitude, and the maximum absolute values of the spin-dependent Seebeck coefficient and spin Seebeck coefficient can reach 550 and 370 μV/K, respectively, when the optimized parameters are used.

2 Model and method

The geometry of the crossed AGNR superlattice p-n junction considered in this paper is shown in Fig. 1. A FM insulator is deposited on top of the entire superlattice. Compared with a graphene-based magnetic superlattice, this type of GNR-based superlattice can be easily fabricated experimentally [53–55]. The system can be divided into three regions: left lead, central region, and right lead. The two semi-infinite leads have perfect periodicity along the ribbon axis with width W_1. The central region is composed of constrictions with size $W_1 \times L_1$ and stubs with size $(W_1 + 2h) \times L_2$. Let n represent the period number of the superlattice. Figure 1 shows the case for $n = 2$, $W_1 = h = 4$, and $L_1 = L_2 = 2$.

A FM insulator is deposited on top of the entire superlattice and induces exchange splitting [56]. To describe the spin transport properties of the AGNRs, one uses the tight-binding Hamiltonian [57, 58]

$$H = \sum_{i,\sigma}(\epsilon_i - \sigma M)a^{\dagger}_{i\sigma}a_{i\sigma} - t\sum_{\langle ij\rangle,\sigma} \mathrm{e}^{\mathrm{i}\phi_{ij}}a^{\dagger}_{i\sigma}a_{j\sigma}, \tag{1}$$

where $\sigma = \uparrow, \downarrow$ represents the up- and down-spin of electrons, respectively, and $a^{\dagger}_{i\sigma}$ ($a_{i\sigma}$) creates (annihilates) an electron on site i. ϵ_i is the on-site energy (i.e., the Dirac-point energy). In the left and right leads, $\epsilon_i = E_L$ or E_R, which can be controlled by the gate voltages. In the central region, the potential drop from the left to the right leads is assumed to be linear, i.e.,

$$\epsilon_i = \begin{cases} \left(\dfrac{3}{2}m + \dfrac{1}{2}\right)(E_R - E_L)/(6L + 2) + E_L, & \text{when } m \text{ is odd;} \\ \dfrac{3}{2}m(E_R - E_L)/(6L + 2) + E_L, & \text{when } m \text{ is even,} \end{cases} \tag{2}$$

where L is the length of the central region, and $m = 0, 1, 2, \ldots, 4L + 1$ (see Fig. 1); Fig. 1 shows the case for $L = 10$. $\boldsymbol{M}$ is the FM exchange split, and t is the nearest-neighbor hopping element. In the presence of a perpendicular magnetic field B, a phase factor Φ_{ij} is added to the hopping element, $\Phi_{ij} = \int_i^j \boldsymbol{A}\cdot \mathrm{d}\boldsymbol{l}/\Phi_0$, with the vector potential $\boldsymbol{A} = (-By, 0, 0)$ and the flux quantum $\Phi_0 = \hbar/e$.

By using the NEGF method and the Landauer–Büttiker formula, the two-terminal spin-resolved trans-

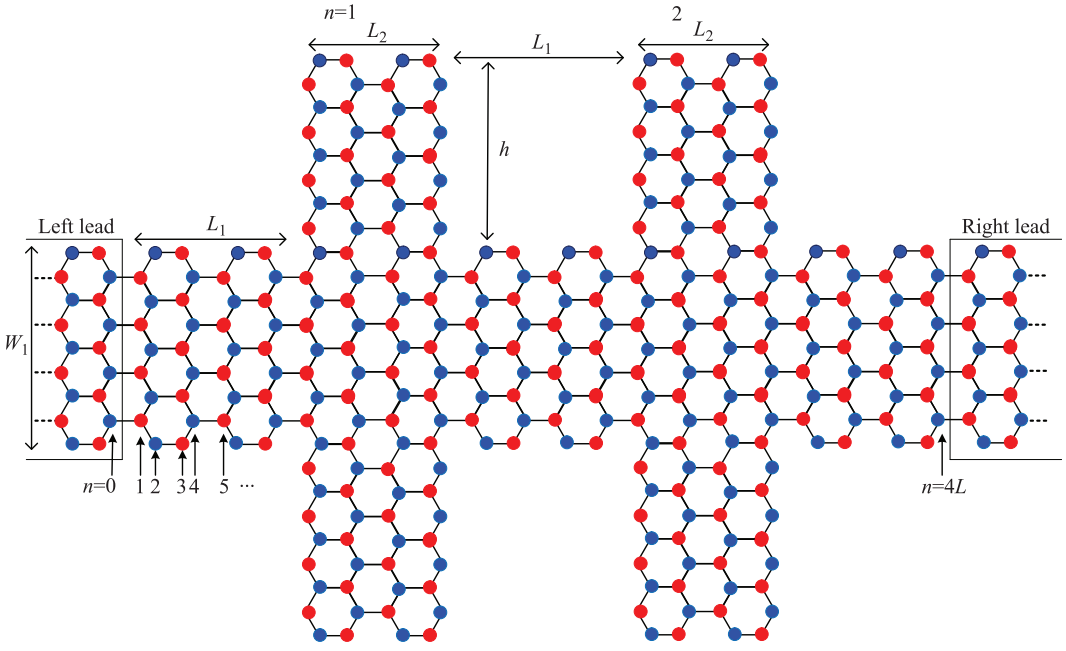

Fig. 1 Schematic illustration of a symmetry crossed superlattice, where a finite central region is connected to two semi-infinite perfect AGNR leads with width W_1. The basic cell consists of a constriction with length L_1 and width W_1 connected to two stubs (top and bottom) with length L_2 and width h. n represents the number of periods of the superlattice. A ferromagnetic insulator is deposited on top of the entire device, and the temperature gradient $\Delta T = T_L - T_R$ is applied to the leads. Blue and red carbon atoms belong to the two distinct sublattices.

mission probability $T_\sigma(E)$ through the AGNR-based superlattice p-n junction is calculated as [50]

$$T_\sigma(E) = \mathbf{Tr}[\Gamma^L_\sigma(E) G^r_\sigma(E) \Gamma^R_\sigma(E) G^a_\sigma(E)], \tag{3}$$

where $G^r_\sigma(E) = [G^a_\sigma(E)]^\dagger = [(E + i\eta)\boldsymbol{I} - H_C - \Sigma^r_{L\sigma} - \Sigma^r_{R\sigma}]^{-1}$ is the retarded Green's function with unit matrix $\boldsymbol{I}$, infinitesimal imaginary $i\eta$, and center scattering region Hamiltonian H_C. Further, $\Sigma^r_{L\sigma(R\sigma)} = H_{CL/R} G^r_{surf,L/R} H^\dagger_{CL/R}$ is the left/right lead's retarded self-energy function with the hopping Hamiltonian $H_{CL/R}$ between the center region and the left/right leads in spin space, and $G^r_{surf,L/R}$ represents the surface Green's functions, which can be calculated numerically [59, 60]. $\Gamma^{L/R}_\sigma$ is the line width function of electrons describing the coupling between the central region and the left/right lead.

It is worth pointing out that actually we need only the retarded Green's function, $G^r_{1,N} = \begin{pmatrix} G^{r\uparrow\uparrow}_{1,N} & 0 \\ 0 & G^{r\downarrow\downarrow}_{1,N} \end{pmatrix}$ of the central region between the leftmost and rightmost layers for a two-probe device (see Fig. 1). The reason is given in a previous work [49]. Further, $G^r_{1,N}$ can be obtained by a recursive algorithm. Here we give the detailed process.

Let the central region consist of N thin slices, as shown in Fig. 1, which are placed at $1, \ldots, N$. Note that the number of sites per slice does not need to be the same for all the slices. We divide a unit cell of an AGNR into four slices. The explicit expressions of the spin-resolved Hamiltonian for the first, second, third, and fourth isolated slices are

$$h^{\uparrow\uparrow/\downarrow\downarrow}_{1,1} = \begin{pmatrix} \epsilon_1 \mp M & 0 & 0 & \ldots & 0 \\ 0 & \epsilon_1 \mp M & 0 & \ddots & 0 \\ 0 & \ddots & \ddots & \ddots & \vdots \\ \vdots & \ddots & 0 & \epsilon_1 \mp M & 0 \\ 0 & \ldots & 0 & 0 & \epsilon_1 \mp M \end{pmatrix}, \tag{4}$$

$$h^{\uparrow\uparrow/\downarrow\downarrow}_{2,2} = \begin{pmatrix} \epsilon_2 \mp M & 0 & 0 & \ldots & 0 \\ 0 & \epsilon_2 \mp M & 0 & \ddots & 0 \\ 0 & \ddots & \ddots & \ddots & \vdots \\ \vdots & \ddots & 0 & \epsilon_2 \mp M & 0 \\ 0 & \ldots & 0 & 0 & \epsilon_2 \mp M \end{pmatrix}, \tag{5}$$

$$h^{\uparrow\uparrow/\downarrow\downarrow}_{3,3} = \begin{pmatrix} \epsilon_3 \mp M & 0 & 0 & \ldots & 0 \\ 0 & \epsilon_3 \mp M & 0 & \ddots & 0 \\ 0 & \ddots & \ddots & \ddots & \vdots \\ \vdots & \ddots & 0 & \epsilon_3 \mp M & 0 \\ 0 & \ldots & 0 & 0 & \epsilon_3 \mp M \end{pmatrix}, \tag{6}$$

$$h^{\uparrow\uparrow/\downarrow\downarrow}_{4,4} = \begin{pmatrix} \epsilon_4 \mp M & 0 & 0 & \ldots & 0 \\ 0 & \epsilon_4 \mp M & 0 & \ddots & 0 \\ 0 & \ddots & \ddots & \ddots & \vdots \\ \vdots & \ddots & 0 & \epsilon_4 \mp M & 0 \\ 0 & \ldots & 0 & 0 & \epsilon_4 \mp M \end{pmatrix}, \tag{7}$$

where $h^{\uparrow\uparrow/\downarrow\downarrow}_{1,1}$ and $h^{\uparrow\uparrow/\downarrow\downarrow}_{4,4}$ are $W_1 \times W_1$ matrices, and $h^{\uparrow\uparrow/\downarrow\downarrow}_{2,2}$ and $h^{\uparrow\uparrow/\downarrow\downarrow}_{3,3}$ are $(W_1 + 1) \times (W_1 + 1)$ matrices. $\uparrow\uparrow$ and $\downarrow\downarrow$ represent up and down spin, respectively, and $\epsilon_1 = 2(E_R - E_L)/(6L + 2) + E_L$, $\epsilon_2 = 3(E_R - E_L)/(6L + 2) + E_L$, $\epsilon_3 = 5(E_R - E_L)/(6L + 2) + E_L$, and $\epsilon_4 = 6(E_R - E_L)/(6L + 2) + E_L$ are caused by the voltage drop in Eq. (2). M is the magnitude of the split energy induced by the FM insulator. In both the spatial and spin spaces, the Hamiltonian $h_{n,n}$ can be written as $h_{n,n} = \begin{pmatrix} h^{\uparrow\uparrow}_{n,n} & 0 \\ 0 & h^{\downarrow\downarrow}_{n,n} \end{pmatrix}$ with $n = 1$, 2, 3, and 4 for the first, second, third, and fourth slices, respectively. First, the $n = 1$ slice can be incorporated to the left lead as follow:

$$G^{(1)r}_{1,1} = (E - h_{1,1} - \Sigma^r_{1,1})^{-1}, \tag{8}$$

where $\Sigma^r_{1,1}$ is the retarded self-energy function for the left lead. Note that this Green's function, $G^{(1)r}_{1,1}$, takes into account the coupling of the first slice with the left lead. Using Dyson's equation [50, 51], we can evaluate the next successive $N - 1$ Green's functions using recurrence formulas as follows:

$$G^{(n)r}_{n,n} = g^r_n + g^r_n h_{n,n-1} G^{(n-1)r}_{n-1,n-1} h_{n-1,n} G^{(n)r}_{n,n}, \tag{9}$$

$$G^{(n)r}_{1,n} = G^{(n-1)r}_{1,n-1} h_{n-1,n} G^{(n)r}_{n,n}, \tag{10}$$

where $g^r_n = (E - h_{n,n})^{-1}$ is the retarded Green's function of the isolated nth slice in the system with $n = 2, \ldots, N$, $h_{n,n-1}$ is the hopping Hamiltonian matrix between the two nearest slices at sites n and $n - 1$, and $h_{n-1,n} = h^\dagger_{n,n-1}$. In the presence of the FM insulator and a perpendicular magnetic field, $h_{n,n-1}$ can be written as $h_{n,n-1} = \begin{pmatrix} h^{\uparrow\uparrow}_{n,n-1} & 0 \\ 0 & h^{\downarrow\downarrow}_{n,n-1} \end{pmatrix}$. The explicit expressions for $h_{n,n-1}$ with $n = 2, \ldots, 5$ are

$$h^{\uparrow\uparrow}_{2,1} = h^{\downarrow\downarrow}_{2,1} = \begin{pmatrix} t & 0 & \ldots & 0 \\ t & t & \ddots & 0 \\ 0 & \ddots & \ddots & \vdots \\ \vdots & \ddots & t & t \\ 0 & \ldots & 0 & t \end{pmatrix}, \tag{11}$$

$$h_{3,2}^{\uparrow\uparrow}=h_{3,2}^{\downarrow\downarrow}=\begin{pmatrix} te^{-i2\Phi} & 0 & 0 & \dots & 0 \\ 0 & te^{-i4\Phi} & 0 & \ddots & 0 \\ 0 & \ddots & \ddots & \ddots & \vdots \\ \vdots & \ddots & 0 & te^{-i2W_1\Phi} & 0 \\ 0 & \dots & 0 & 0 & te^{-i2(W_1+1)\Phi} \end{pmatrix}, \tag{12}$$

$$h_{4,3}^{\uparrow\uparrow}=h_{4,3}^{\downarrow\downarrow}=\begin{pmatrix} t & t & 0 \dots & 0 \\ 0 & t & t & \ddots & 0 \\ \vdots & \ddots & t & t & 0 \\ 0 & \dots & 0 & t & t \end{pmatrix}, \tag{13}$$

$$h_{5,4}^{\uparrow\uparrow}=h_{5,4}^{\downarrow\downarrow}=\begin{pmatrix} te^{-i2\Phi} & 0 & 0 & \dots & 0 \\ 0 & te^{-i4\Phi} & 0 & \ddots & 0 \\ 0 & \ddots & \ddots & \ddots & \vdots \\ \vdots & \ddots & 0 & te^{-i2(W_1-1)\Phi} & 0 \\ 0 & \dots & 0 & 0 & te^{-i2W_1\Phi} \end{pmatrix}, \tag{14}$$

where $\Phi = (3\sqrt{3}/4)a^2B/\Phi_0$ is the magnetic flux for the carbon-carbon distance $a = 0.142$ nm. The method of choosing the above Hamiltonian ensures that the magnetic flux through each honeycomb lattice of graphene is 2Φ when a uniform perpendicular magnetic field is applied. Further, $h_{2,1}$, $h_{3,2}$, $h_{4,3}$, and $h_{5,4}$ are $(W_1+1)\times W_1$, $(W_1+1)\times(W_1+1)$, $W_1\times(W_1+1)$, and $W_1\times W_1$ matrices, respectively. After $N-1$ inversions, we can obtain the Green's functions $G_{1,N}^{(N)r}$ and $G_{N,N}^{(N)r}$. Note that the dimensions of $h_{n+1,n}$ and $h_{n,n}$ need to be broadened in the presence of stubs. Finally, we need to incorporate the self-energy of the right lead into $G_{1,N}^{(N)r}$ and $G_{N,N}^{(N)r}$; we can apply Dyson's equation again, obtaining

$$G_{N,N}^{r} = [(G_{N,N}^{(N)r})^{-1} - \Sigma_{N,N}^{r}]^{-1}, \tag{15}$$

$$G_{1,N}^{r} = G_{1,N}^{(N)r} + G_{1,2L+1}^{(N)r}\Sigma_{N,N}^{r}G_{N,N}^{r}. \tag{16}$$

Then, with the spin-resolved transmission probability $T_\sigma(E)$ at hand, we can calculate the spin-dependent Seebeck coefficient using the following formula [61–63]:

$$S_\sigma(E_F) = \frac{1}{eT}\frac{\int_{-\infty}^{+\infty} dE(E-E_F)\boldsymbol{T}_\sigma(E)f(1-f)}{\int_{-\infty}^{+\infty} dE\boldsymbol{T}_\sigma(E)f(1-f)}, \tag{17}$$

where $f(E,E_F,T) = [e^{(E-E_F)/(k_BT)}+1]^{-1}$ is the Fermi distribution function at the Fermi energy E_F and temperature T. Using these quantities, the spin Seebeck coefficient S_S is calculated as [61, 62]

$$S_S(E_F) = \frac{1}{2}(S_\uparrow - S_\downarrow). \tag{18}$$

3 Results and discussion

In the following, we present some numerical examples of the calculated spin-dependent transmission probability T_σ, spin-dependent Seebeck coefficient S_σ, and spin Seebeck coefficient S_S for the p-n junctions shown in Fig. 1. We consider two systems: (1) a crossed AGNR superlattice p-n junction with width $W_1 = 40$ (∼9.8 nm) and (2) a crossed AGNR superlattice p-n junction with width $W_1 = 41$ (∼10.1 nm). The former is semiconducting and the latter is metallic for pristine AGNRs. Here, we emphasize whether the two systems still have semiconducting or metallic properties in the presence of stubs. In the calculation, the hopping energy is set to $t = 2.75$ eV. The magnetic field B is expressed in terms of the magnetic flux Φ with $\Phi = (3\sqrt{3}/4)a^2B/\Phi_0$, and Φ is proportional to B. Thus, the parameter Φ can be used to define the strength of the magnetic field B. The temperature T is fixed at 300 K.

In Figs. 2(a)–(c) and (b′), (c′), we present the spin Seebeck coefficient S_S (in units of μV/K), the spin-up Seebeck coefficient $S_\uparrow$ and spin-down Seebeck coefficient $S_\downarrow$, and the spin-dependent transmission probability $T_\uparrow$ and $T_\downarrow$, respectively, versus the Fermi energy E_F (in units of eV) at zero magnetic field ($\Phi = 0$) for lengths $L_1 = L_2 = 10$ and a stub width $h = 20$ with magnetization $M = 0.1$ eV and different potential drops for a crossed AGNR superlattice p-n junction with width $W_1 = 40$ and $n = 10$ periods. Figs. 2(d)–(f) correspond to Figs. 2(a)–(c), and Figs. 2(e′), (f′) correspond to Figs. 2(b′), (c′), respectively, but for a crossed superlattice p-n junction with width $W_1 = 41$. First, it is clear that $T_\uparrow$ and $T_\downarrow$ for both p-n junctions present a series of peaks at defined Fermi energies. This resonant behavior of the electronic transmission probability arises from interference of the electronic wave functions inside the structure, which travels back and forth forming stationary states in the conductor region. Furthermore, one can find that the degeneracy of the two spin-dependent transmission probability T_σ is eliminated by the exchange splitting M. The spin-up (-down) transmission probability profiles shift in opposite directions, and the total translational distance should be $2M$ [see Figs. 2(b′), (c′) and (e′), (f′)]. For a p-n junction with electron-hole symmetry and $E_L = -E_R$, both $T_\uparrow$ and $T_\downarrow$ for the two systems near $E_F = 0$ are enhanced, with more resonant peaks as the potential drop $\Delta V = E_L - E_R$ increases in Figs. 2(b′), (c′) and (e′), (f′) and their insets. This enhancement is particularly obvious for a crossed p-n junction with width $W_1 = 41$ owing to the increased concentration of electrons or holes. When E_F is far from the Dirac point, $T_\uparrow$ and $T_\downarrow$ for the two systems decrease dramatically with increasing potential drop ΔV owing to

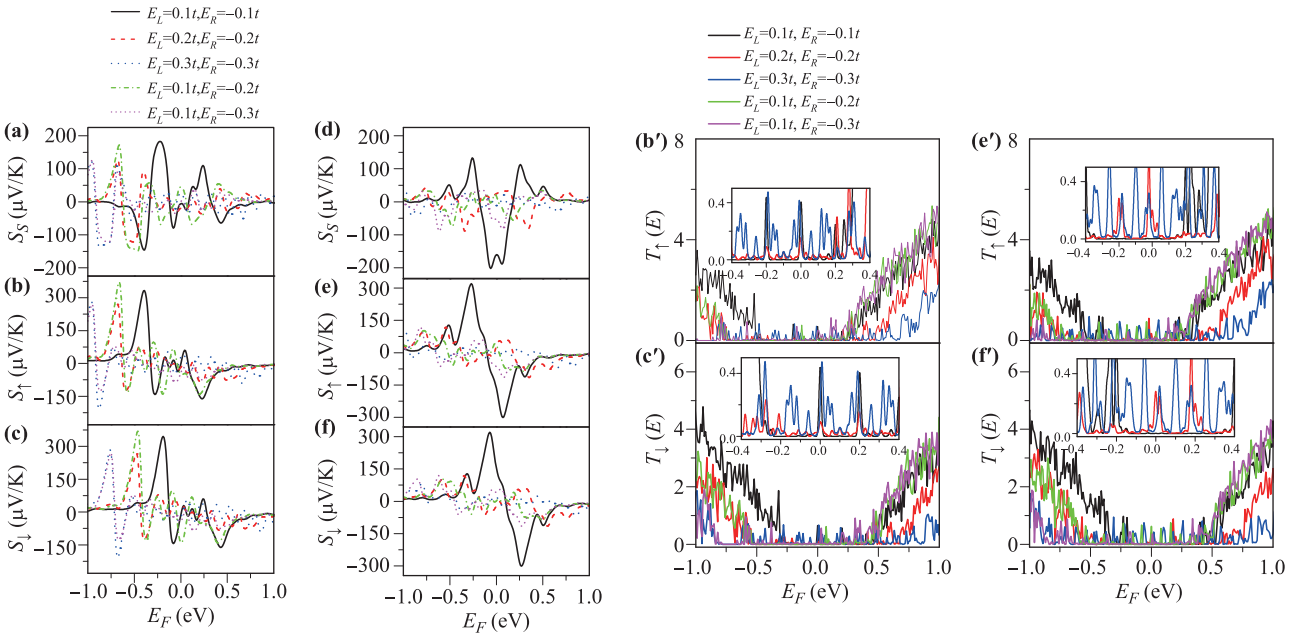

Fig. 2 **(a)** Spin Seebeck coefficient S_S, **(b)** spin-up Seebeck coefficient $S_\uparrow$ and **(b′)** transmission probability $T_\uparrow$, and **(c)** spin-down Seebeck coefficient $S_\downarrow$ and **(c′)** transmission probability $T_\downarrow$ as a function of the Fermi energy E_F with different potential drops in the central region for a symmetry crossed superlattice with $W_1 = 40$. **(d)**–**(f)** correspond to **(a)**–**(c)**, and **(e′)**, **(f′)** correspond to **(b′)**, **(c′)**, respectively, but for $W_1 = 41$. The parameters are taken as $\Phi = 0$, $M = 0.1$ eV, $n = 10$, $h = 20$, and $L_1 = L_2 = 10$. The insets in **(b′)**, **(c′)** and **(e′)**, **(f′)** show $T_\uparrow$ and $T_\downarrow$ for -0.4 eV $\leq E_F \leq 0.4$ eV, respectively.

scattering of the electronic wave caused by the p-n interface. A similar result has also been obtained for a ZGNR p-n junction and a crossed ZGNR superlattice p-n junction [49, 64]. For $E_L \neq -E_R$ [see (green) solid lines and (magenta) solid lines in Figs. 2(b′), (c′) and (e′), (f′)], $T_\uparrow$ and $T_\downarrow$ remain essentially unchanged when E_F is greater than $E_L = 0.1t$, and they are reduced remarkably for $E_F < -0.2t$ as E_R decreases from $-0.2t$ to $-0.3t$ owing to breaking of the electron-hole symmetry. These properties are similar for the two systems. However, a crossed AGNR superlattice p-n junction with width $W_1 = 40$ always shows metallic behavior regardless of the voltage drop magnitude owing to the nonzero transmission values of both $T_\uparrow$ and $T_\downarrow$ at $E_F = 0$. This metallic behavior can also be understood according to the spin-dependent density of states (DOS) ρ_σ. From Figs. 3(a) and (b) for a crossed AGNR superlattice p-n junction with width $W_1 = 40$, there are clearly nonzero energy states around $E_F = 0$ for both $\rho_\uparrow$ and $\rho_\downarrow$ regardless of ΔV. For the junction with width $W_1 = 41$, as shown in Figs. 2(e′) and (f′) and their insets, the system exhibits semiconducting behavior at a voltage drop of $\Delta V = 0.2t$ [(black) solid lines] because both $T_\uparrow$ and $T_\downarrow$ at $E_F = 0$ are zero. When ΔV increases to $0.4t$ [(red) solid lines], a semiconductor-to-metal transition occurs, and finite values of both $T_\uparrow$ and $T_\downarrow$ appear at $E_F = 0$. To understand the origin of the transition, the spin-dependent DOS ρ_σ versus the

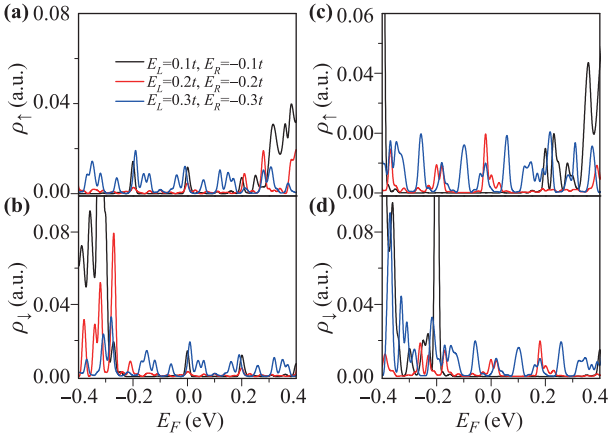

Fig. 3 **(a)** Spin-up and **(b)** spin-down DOS as a function of the Fermi energy E_F with different potential drops in the central region for a symmetry crossed superlattice with $W_1 = 40$. **(c)**, **(d)** correspond to (a), (b), respectively, but for $W_1 = 41$. The other parameters are the same as those in Fig. 2.

Fermi energy E_F for a crossed AGNR superlattice p-n junction with width $W_1 = 41$ is shown in Figs. 3(c) and (d). A gap with a zero value of the DOS clearly disappears around $E_F = 0$ for both $\rho_\uparrow$ and $\rho_\downarrow$ as ΔV increases from $0.2t$ to $0.4t$, producing the semiconductor-to-metal transition.

Further, both $S_\uparrow$ and $S_\downarrow$ for both crossed superlattice p-n junctions also display oscillation similar to that of the spin-dependent transmission coefficient T_σ. The zero values of $S_\uparrow$ ($S_\downarrow$) for both systems are located at the peaks or dips of $T_\uparrow$ ($T_\downarrow$), and the maximal values of $|S_\sigma|$ are located at the positions where T_σ varies sharply. This behavior of S_σ can be easily understood considering that the values of S_σ are approximately determined by the derivative of T_σ at lower temperatures [65]. Therefore, $|S_\sigma|$ is almost zero at peaks or dips of T_σ because the derivative of T_σ is zero, whereas it is maximal when the derivative of T_σ is maximal. Furthermore, it is worth noting that S_σ for both systems reaches the same order of magnitude, and its maximum absolute value reaches 335 μV/K when $E_L = -E_R = 0.1$ eV. This maximum value of S_σ is caused by the appearance of a zero transmission gap for T_σ [see Figs. 2(b′), (c′) and (e′), (f′)] for the two junctions. Let us look in more detail at the origin of these maximum values. For a crossed superlattice p-n junction with width $W_1 = 40$, a zero transmission gap near $E_F = -0.4$ eV ($E_F = -0.2$) appears in the spin-up (spin-down) channel, as shown in the lower part of Figs. 2(b′) and (c′) and their insets. At the edges of this gap, transport in the up- and down-spin channels is mediated by thermally activated holes or electrons, which leads to a large positive or negative S_σ. For a crossed superlattice p-n junction with width $W_1 = 41$, a wider zero transmission gap appears around $E_F = 0$ for both $S_\uparrow$ and $S_\downarrow$ [see Figs. 2(e′) and (f′) and their insets], so a large positive or negative S_σ also appears at the edges of these gaps. When the potential drop ΔV is increased from $0.2t$ [(black) solid lines] to $0.6t$ [(blue) dotted lines] in Figs. 2(b) and (c), the maximum values of S_σ shift toward negative E_F owing to the leftward shift of the zero transmission gaps of both $T_\uparrow$ and $T_\downarrow$ for a junction with $W_1 = 40$. In contrast, the maximum value of S_σ decreases dramatically because the zero transmission gaps vanish for a junction with $W_1 = 41$ [see Figs. 2(e′) and (f′) and their insets]. The result obtained here is different from that of Refs. [11, 12], and [66] for a pristine GNR system, where the Seebeck coefficient for semiconducting AGNR systems is much larger than that for metallic AGNR systems. However, the maximum values of the Seebeck coefficient are of the same order of magnitude regardless of whether the AGNR junction is metallic or semiconducting in the presence of stubs. Further, as seen in Figs. 2(a) and (d), the variation of the spin Seebeck coefficient S_S for both systems shows a tendency similar to that of S_σ according to Eq. (18).

As the magnetization M is increased for the crossed superlattice p-n junctions shown in Figs. 4(b′), (c′) and (e′), (f′), the relative shift of the spin-dependent transmission probabilities $T_\uparrow$ and $T_\downarrow$ with respect to the Dirac point for the two systems increases, but the magnitude of $T_\uparrow$ and $T_\downarrow$ for the two systems remains essentially unchanged. As a result, the magnitudes of both the spin-up Seebeck coefficient $S_\uparrow$ and spin-down Seebeck coefficient $S_\downarrow$ also remain unchanged, and only the positions of both

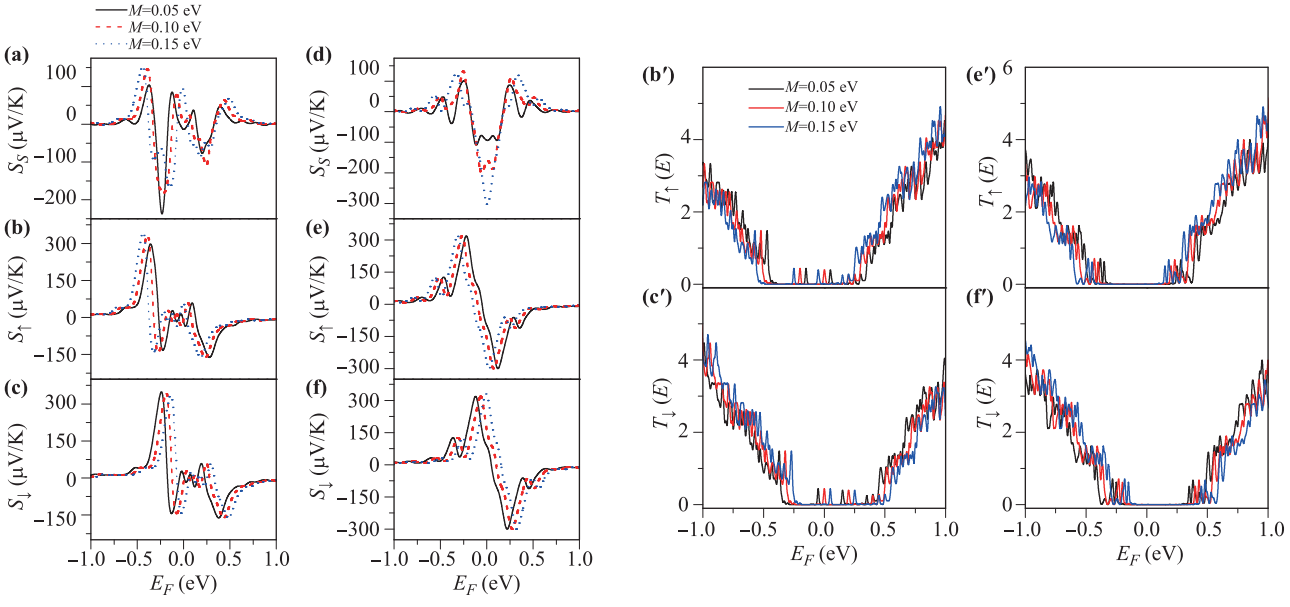

Fig. 4 **(a)** Spin Seebeck coefficient S_S, **(b)** spin-up Seebeck coefficient $S_\uparrow$ and **(b′)** transmission probability $T_\uparrow$, and **(c)** spin-down Seebeck coefficient $S_\downarrow$ and **(c′)** transmission probability $T_\downarrow$ as a function of the Fermi energy E_F for different magnetizations M and $E_L = -E_R = 0.1t$ for a symmetry crossed superlattice with $W_1 = 40$. **(d)**, **(f)** correspond to **(a)**, **(c)**, and **(e′)**, **(f′)** correspond to **(b′)**, **(c′)**, respectively, but for $W_1 = 41$. The other parameters are the same as those in Fig. 2.

$S_\uparrow$ and $S_\downarrow$ shift with M because S_σ is approximately determined by the derivative of T_σ at low temperatures, as discussed in connection with Fig. 2. One can see this clearly from Figs. 4(b), (c) and (e), (f). These properties are similar for the two systems. However, there is an essential difference in behavior. For a crossed AGNR superlattice p-n junction with width $W_1 = 40$, the spin Seebeck coefficient S_S is insensitive to the magnetization M [see Fig. 4(a)] owing to the metallic behavior of the junction, whereas S_S increases rapidly around zero Fermi energy E_F for a junction with width $W_1 = 41$ [see Fig. 4(d)] as M increases from 0.05 to 1.5 eV. A similar phenomenon has also been observed for a crossed ZGNR superlattice p-n junction [49]. The above behavior of S_S can be easily understood considering the spin-dependent transmission coefficient presented in Figs. 4(e′) and (f′), where a zero transmission gap appears around zero Fermi energy for both $T_\uparrow$ and $T_\downarrow$. Thus, a finite spin transmission gap with zero value can appear and increase with increasing M. As a result, S_S is also enhanced because it scales linearly with the spin transmission gap [18].

Next, we present the spin Seebeck coefficient S_S, the spin-dependent Seebeck coefficient S_σ, and the spin-dependent transmission probability T_σ versus the Fermi energy E_F for different numbers n of periods of the superlattice at a given magnetization $M = 0.1$ eV in Fig. 5. Figures 5(a)–(c) and (d)–(f) show the results for crossed superlattice p-n junctions with widths $W_1 = 40$ and $W_1 = 41$, respectively. Figures 5(b′), (c′) and (e′), (f′) correspond to the spin-dependent transmission probability for the two cases. The other parameters are the same as those in Fig. 2. An important result in Fig. 5(a) is that $|S_S|$ around zero Fermi energy for the crossed superlattice p-n junction with width $W_1 = 40$ is remarkably enhanced with increasing n, and the maximum absolute value reaches 380 μV/K for $n = 20$. The increase in $|S_S|$ is somewhat visible at the corresponding peaks and dips. A similar phenomenon in which S_S is proportional to n has also been obtained for a crossed superlattice p-n junction with a zigzag edge [49]. For a crossed superlattice p-n junction with width $W_1 = 41$, $|S_S|$ around zero Fermi energy also increases when n increases, and a maximum $|S_S|$ value of 320 μV/K is realized when $n = 15$, but $|S_S|$ decreases as n increases further to 20. This difference in the behavior of S_S in the two cases can be easily understood considering the spin-dependent transmission spectra presented in Figs. 5(b′), (c′) and (e′), (f′). From Figs. 5(a′) and (b′), we can see that a metal-to-semiconductor transition occurs for a crossed superlattice junction with $W_1 = 40$ as n increases from 5 to 15. An obvious zero transmission gap appears near $E_F = 0$ at $n = 15$ for both $T_\uparrow$ and $T_\downarrow$. As n increases further from 15 [(blue) solid lines] to 20 [(green) solid lines], the zero transmission gaps for $T_\uparrow$ and $T_\downarrow$ are broadened. Therefore, both $S_\uparrow$ and $S_\downarrow$ are notably enhanced. According to Eq. (18), the variation in S_S has a tendency similar to that of S_σ, which leads to the enhancement of S_S as n increases. The explanation of the origin of the

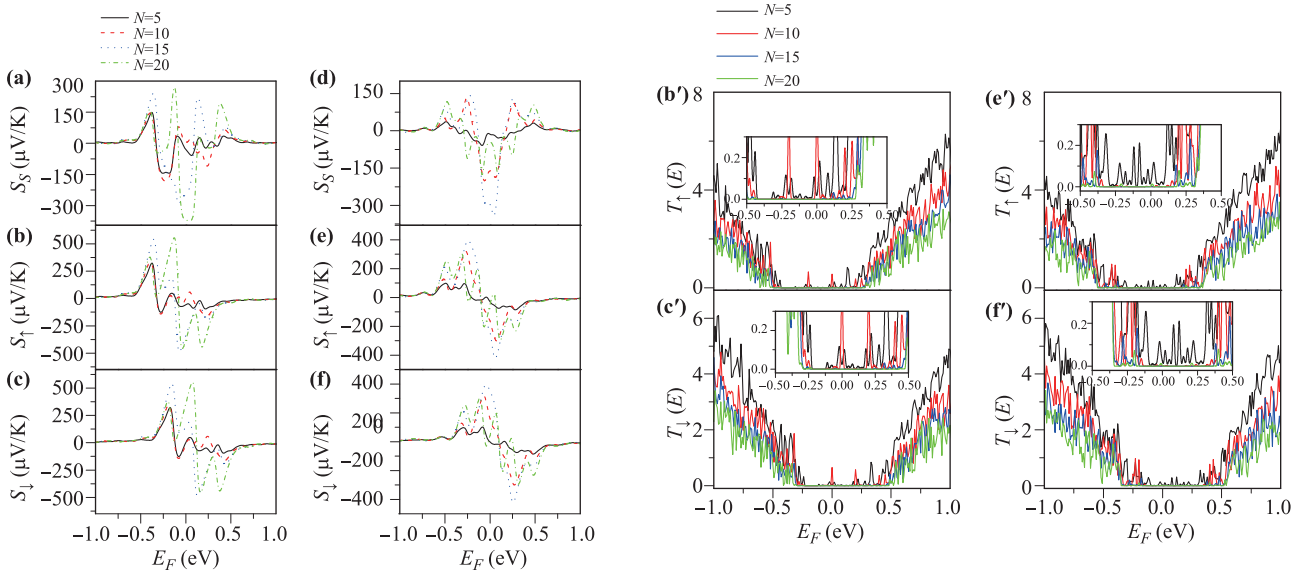

Fig. 5 **(a)** Spin Seebeck coefficient S_S, **(b)** spin-up Seebeck coefficient $S_\uparrow$ and **(b′)** transmission probability $T_\uparrow$, and **(c)** spin-down Seebeck coefficient $S_\downarrow$ and **(c′)** transmission probability $T_\downarrow$ as a function of the Fermi energy E_F with a different number n of periods of the superlattice under $E_L = -E_R = 0.1t$ for a symmetry crossed superlattice with $W_1 = 40$. **(d)**–**(f)** correspond to **(a)**–**(c)**, and **(e′)**, **(f′)** correspond to **(b′)**, **(c′)**, respectively, but for $W_1 = 41$. The other parameters are the same as those in Fig. 2. The insets in **(b′)**, **(c′)** and **(e′)**, **(f′)** show $T_\uparrow$ and $T_\downarrow$, respectively, for -0.5 eV $\leq E_F \leq 0.5$ eV.

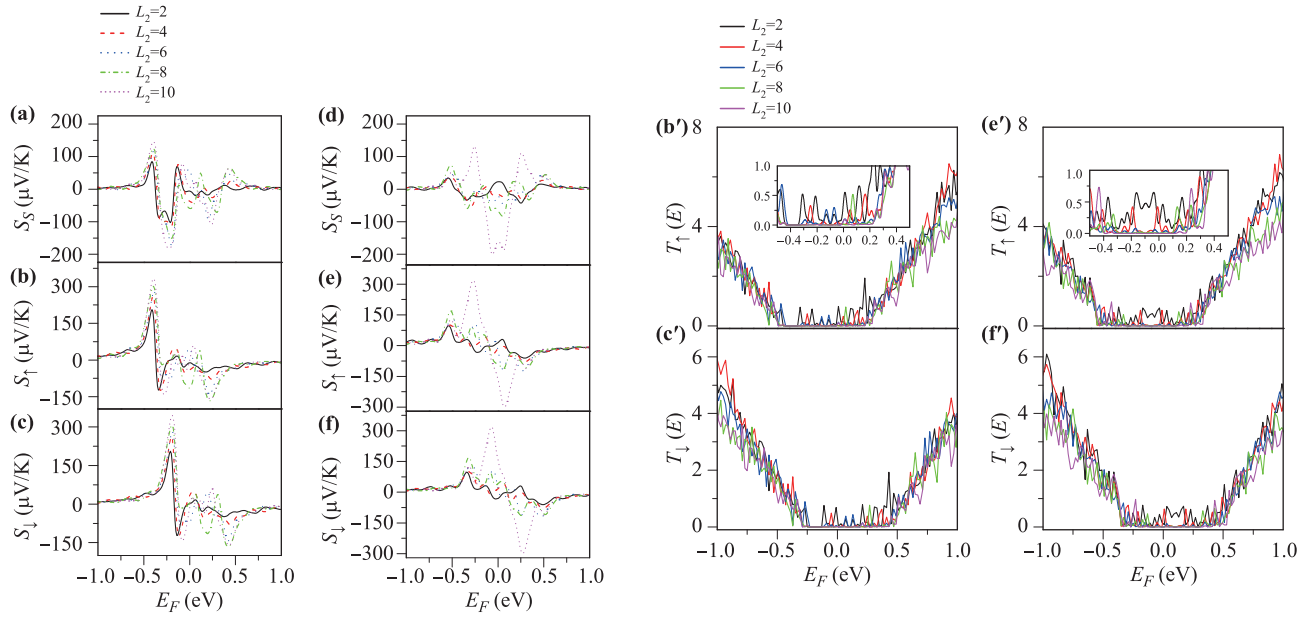

Fig. 6 **(a)** Spin Seebeck coefficient S_S, **(b)** spin-up Seebeck coefficient $S_\uparrow$ and **(b′)** transmission probability $T_\uparrow$, and **(c)** spin-down Seebeck coefficient $S_\downarrow$ and **(c′)** transmission probability $T_\downarrow$ as a function of the Fermi energy E_F with different stub lengths L_2 under $E_L = -E_R = 0.1t$ for a symmetry crossed superlattice with $W_1 = 40$. **(d)**–**(f)** correspond to **(a)**–**(c)**, and **(e′)**, **(f′)** correspond to **(b′)**, **(c′)**, respectively, but for $W_1 = 41$. The other parameters are the same as those in Fig. 2. The insets in **(b′)** and **(e′)** show $T_\uparrow$ for -0.4 eV $\leq E_F \leq 0.4$ eV.

enhancement of S_S for the crossed superlattice junction with $W_1 = 41$ is similar to that presented above for a junction with $W_1 = 40$ as n increases from 5 to 15, but finite values of both $T_\uparrow$ and $T_\downarrow$ appear around $E_F = 0$ as n increases from 15 to 20, as shown in Figs. 5(e′) and (f′) and their insets. Consequently, both $S_\uparrow$ and $S_\downarrow$ are significantly decreased, which also leads to a remarkable reduction in S_S.

Now we focus on the effects of the stub length on the spin-dependent transport and thermoelectric properties of the systems. Figure 6 shows the spin Seebeck coefficient S_S, spin-dependent Seebeck coefficient S_σ, and spin-dependent transmission probability T_σ as a function of the Fermi energy E_F for different stub lengths L_2 and $n = 10$ periods of the superlattice for crossed superlattice p-n junctions with width $W_1 = 40$ and 41. The other parameters are the same as those in Fig. 5. One can clearly see that the increase in L_2 considerably enhances S_S and S_σ at certain Fermi energy values for the two junctions. This enhancement is due mainly to the rapid increase or decrease in the spin-dependent transmission probability T_σ or the appearance of an enlarged zero transmission gap for T_σ. The most remarkable changes in both $T_\uparrow$ and $T_\downarrow$ can be observed for the crossed superlattice p-n junctions with $W_1 = 41$ in Figs. 6(e′) and (f′), where both $T_\uparrow$ and $T_\downarrow$ reach zero at zero Fermi energy, leading to a metal-to-semiconductor transition as L_2 increases from 8 to 10. Further, a transmission gap of ∼0.42 eV also appears for both $T_\uparrow$ and $T_\downarrow$. According to the explanation of Fig. 2, both S_S and S_σ reveal high peaks when the Fermi energy is in the energy gap. For larger $|E_F|$, the transmission curves in Figs. 6(b′), (c′) and (e′), (f′) exhibit complex behavior when L_2 is increased, and S_S and S_σ depend weakly on the stub length.

Finally, in Figs. 7(a)–(c) and (b′), (c′), we present the spin Seebeck coefficient S_S (in units of μV/K), the spin-dependent Seebeck coefficients $S_\uparrow$ and $S_\downarrow$, and the spin-dependent transmission probabilities $T_\uparrow$ and $T_\downarrow$, respectively, versus the Fermi energy E_F (in units of eV) at a potential of $E_L = -E_R = 0.1t$ and stub lengths $L_1 = L_2 = 10$ and heights $h = 20$ with a magnetization M of 0.1 eV under different magnetic fields Φ for a crossed superlattice p-n junction with width $W_1 = 40$ and $n = 10$ periods. Figures 7(d)–(f) correspond to Figs. 7(a)–(c), and Figs. 7(e′), (f′) correspond to Figs. 7(b′), (c′), respectively, but for a crossed superlattice p-n junction with width $W_1 = 41$. In Figs. 7(b′), (c′) and (e′), (f′), we can see that in the presence of the magnetic field, both $T_\uparrow$ and $T_\downarrow$ for the two systems increase notably near $E_F = 0$, and the transmission gap of $T_\uparrow$ and $T_\downarrow$ for the two systems disappears, especially for the superlattice junction with width $W_1 = 41$, where a semiconductor-to-metal transition occurs as the magnetic field Φ increases from 0 to 0.003 [see Figs. 7(e′) and (f′) and the inset in Fig. 7(e′)]. This disappearance of the transmission gaps can be expected to strongly sup-

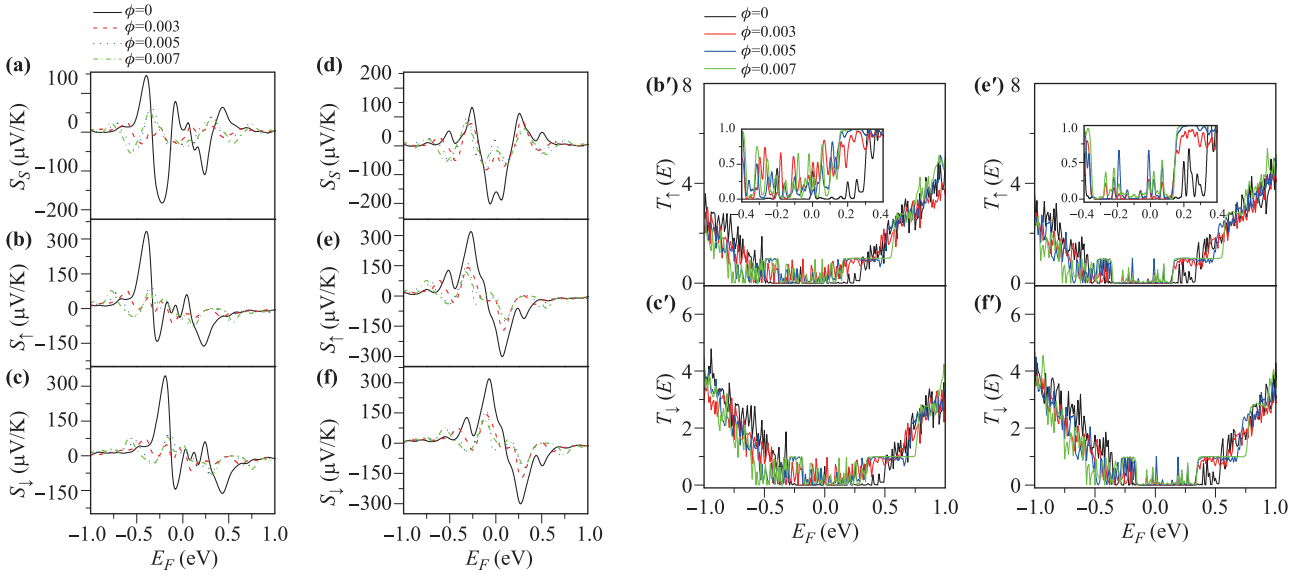

Fig. 7 **(a)** Spin Seebeck coefficient S_S, **(b)** spin-up Seebeck coefficient $S_\uparrow$ and **(b′)** transmission probability $T_\uparrow$, and **(c)** spin-down Seebeck coefficient $S_\downarrow$ and **(c′)** transmission probability $T_\downarrow$ as a function of the Fermi energy E_F for different magnetic fluxes Φ under $E_L = -E_R = 0.1t$ for a symmetry crossed superlattice with $W_1 = 40$. **(d)**–**(f)** correspond to **(a)**–**(c)**, and **(e′)**, **(f′)** correspond to **(b′)**, **(c′)**, respectively, but for $W_1 = 41$. The other parameters are the same as those in Fig. 2. The insets in **(b′)** and **(e′)** show $T_\uparrow$ for -0.4 eV $\leq E_F \leq 0.4$ eV.

press $S_\uparrow$ and $S_\downarrow$ [see Figs. 7(b), (c) and (e), (f)] according to the above discussion. Thus, S_S is also remarkably reduced in the presence of the magnetic field. When Φ increases further, as shown in Figs. 7(b′), (c′) and (e′), (f′), the magnitudes of both $T_\uparrow$ and $T_\downarrow$ for the two systems remain essentially invariant near $E_F = 0$, and both $T_\uparrow$ and $T_\downarrow$ display irregular oscillation. When Φ increases to 0.007 [(green) solid lines in Figs. 7(b′), (c′) and (e′), (f′) and their insets], the Landau levels are formed from the Dirac point to the high Fermi energy [67]. Thus, the properties of S_S and S_σ for the two systems tend to be the same. Further, it is worth noting that from Figs. 7(b′), (c′) and (e′), (f′), the magnitudes of both $T_\uparrow$ and $T_\downarrow$ in both systems are nearly independent of Φ when E_F is far from the Dirac point. This result is different from that of Ref. [49] for a crossed superlattice p-n junction with a zigzag edge, where both $T_\uparrow$ and $T_\downarrow$ decrease gradually with increasing Φ. The result indicates that the transport properties depend strongly on the chirality of the graphene ribbon.

4 Summary and conclusion

In summary, we comprehensively studied the spin-dependent transport and Seebeck effects for crossed superlattice p-n junctions based on an AGNR with width $W_1 = 40$ and 41 to exemplify the effect of semiconducting and metallic AGNRs, respectively. Our results revealed that in the presence of stubs, a semiconducting AGNR junction with width $W_1 = 40$ always shows metallic behavior regardless of the potential drop magnitude, magnetization strength, stub length, and perpendicular magnetic field strength. However, a metallic AGNR junction with width $W_1 = 41$ can present metallic or semiconducting behavior depending on the physical parameters mentioned above. Furthermore, a metal-to-semiconductor transition can be realized in both systems by adjusting the number of periods of the superlattice. In addition, the spin-dependent Seebeck coefficient and spin Seebeck coefficient for the crossed superlattice p-n junctions with widths W_1 of 40 and 41 are of the same order of magnitude when the system parameters are optimized, and the maximum absolute values of the spin-dependent Seebeck coefficient and spin Seebeck coefficient reach 550 and 370 μV/K, respectively. However, we should mention that the electron transport and thermoelectric properties of a T-shaped superlattice p-n junction are similar to those of a crossed one, so the results are not shown here. Our findings may provide valuable guidance for the design and fabrication of spin valve and high-performance thermoelectric devices based on a GNR superlattice p-n junction in practical applications.

Acknowledgements This work was supported by the National Natural Science Foundation of China (Grant Nos. 11704118, 11774085, and 11404230), the Scientific Research Fund of Hunan Provincial Education Department (Grant Nos. 17A193 and

17C0946), the Hunan Provincial Natural Science Foundation of China (Grant No. 2017JJ3210), and the Foundation of Science and Technology Bureau of Sichuan Province (No. 2013JY0085).

References

1. F. J. DiSalvo, Thermoelectric cooling and power generation, *Science* 285(5428), 703 (1999)
2. R. Mahajan, Chia-pin Chiu, and G. Chrysler, Cooling a microprocessor chip, *Proc. IEEE* 94(8), 1476 (2006)
3. C. B. Vining, An inconvenient truth about thermoelectrics, *Nat. Mater.* 8(2), 83 (2009)
4. A. Banerjee, B. Fauque, K. Izawa, A. Miyake, I. Sheikin, J. Flouquet, B. Lenoir, and K. Behnia, Transport anomalies across the quantum limit in semimetallic $Bi_{0.96}Sb_{0.04}$, *Phys. Rev. B* 78(16), 161103(R) (2008)
5. C. Hohn, M. Galffy, and A. Freimuth, Resistivity, Hall effect, Nernst effect, and thermopower in the mixed state of $La_{1.85}Sr_{0.15}CuO_4$, *Phys. Rev. B* 50(21), 15875 (1994)
6. J. P. Small, K. M. Perez, and P. Kim, Modulation of thermoelectric power of individual carbon nanotubes, *Phys. Rev. Lett.* 91(25), 256801 (2003)
7. Y. M. Zuev, W. Chang, and P. Kim, Thermoelectric and magnetothermoelectric transport measurements of graphene, *Phys. Rev. Lett.* 102(9), 096807 (2009)
8. P. Wei, W. Bao, Y. Pu, C. N. Lau, and J. Shi, Anomalous thermoelectric transport of Dirac particles in graphene, *Phys. Rev. Lett.* 102(16), 166808 (2009)
9. J. G. Checkelsky and N. P. Ong, Thermopower and Nernst effect in graphene in a magnetic field, *Phys. Rev. B* 80(8), 081413(R) (2009)
10. D. Dragoman and M. Dragoman, Giant thermoelectric effect in graphene, *Appl. Phys. Lett.* 91(20), 203116 (2007)
11. Y. Ouyang and J. Guo, A theoretical study on thermoelectric properties of graphene nanoribbons, *Appl. Phys. Lett.* 94(26), 263107 (2009)
12. Y. X. Xing, Q. F. Sun, and J. Wang, Nernst and Seebeck effects in a graphene nanoribbon, *Phys. Rev. B* 80(23), 235411 (2009)
13. K. Uchida, S. Takahashi, K. Harii, J. Ieda, W. Koshibae, K. Ando, S. Maekawa, and E. Saitoh, Observation of the spin Seebeck effect, *Nature* 455(7214), 778 (2008)
14. M. G. Zeng, W. Huang, and G. C. Liang, Spin-dependent thermoelectric effects in graphene-based spin valves, *Nanoscale* 5(1), 200 (2013)
15. M. G. Zeng, Y. P. Feng, and G. C. Liang, Graphene-based spin caloritronics, *Nano Lett.* 11(3), 1369 (2011)
16. S. G. Cheng, Spin thermopower and thermoconductance in a ferromagnetic graphene nanoribbon, *J. Phys. Condens. Matter* 24(38), 385302 (2012)
17. Y. S. Liu, X. F. Wang, and F. Chi, Non-magnetic doping induced a high spin-filter efficiency and large spin Seebeck eFFect in zigzag graphene nanoribbons, *J. Mater. Chem. C Mater. Opt. Electron. Devices* 1(48), 8046 (2013)
18. X. B. Chen, Y. Z. Liu, B.-L. Gu, W. H. Duan, and F. Liu, Giant room-temperature spin caloritronics in spinsemiconducting graphene nanoribbons, *Phys. Rev. B* 90(12), 121403(R) (2014)
19. R. Venkatasubramanian, E. Siivola, T. Colpitts, and B. O'Quinn, Thin-film thermoelectric devices with high room-temperature figures of merit, *Nature* 413(6856), 597 (2001)
20. A. I. Hochbaum, R. K. Chen, R. D. Delgado, W. J. Liang, E. C. Garnett, M. Najarian, A. Majumdar, and P. D. Yang, Enhanced thermoelectric performance of rough silicon nanowires, *Nature* 451, 163 (2008)
21. Y. S. Liu and Y. C. Chen, Seebeck coefficient of thermoelectric molecular junctions: First-principles calculations, *Phys. Rev. B* 79(19), 193101 (2009)
22. Y. S. Liu, Y. R. Chen, and Y. C. Chen, Thermoelectric efficiency in nanojunctions: A comparison between atomic junctions and molecular junctions, *ASC Nano* 3(11), 3497 (2009)
23. Y. S. Liu, X. F. Yang, X. H. Fan, and Y. J. Xia, Transport properties of a Kondo dot with a larger side-coupled noninteracting quantum dot, *J. Phys. Condens. Matter* 20(13), 135226 (2008)
24. Z. X. Xie, L. M. Tang, C. N. Pan, K. M. Li, K. Q. Chen, and W. H. Duan, Enhancement of thermoelectric properties in graphene nanoribbons modulated with stub structures, *Appl. Phys. Lett.* 100(7), 073105 (2012)
25. F. Mazzamuto, V. Hung Nguyen, Y. Apertet, C. Caër, C. Chassat, J. Saint-Martin, and P. Dollfus, Enhanced thermoelectric properties in graphene nanoribbons by resonant tunneling of electrons, *Phys. Rev. B* 83(23), 235426 (2011)
26. V. T. Tran, J. Saint-Martin, and P. Dollfus, High thermoelectric performance in graphene nanoribbons by graphene/BN interface engineering, *Nanotechnology* 26(49), 495202 (2015)
27. J. W. Li, B. Wang, Y. J. Yu, Y. D. Wei, Z. Z. Yu, and Y. Wang, Spin-resolved quantum transport in graphene-based nanojunctions, *Front. Phys.* 12(4), 126501 (2017)
28. T. Gunst, T. Markussen, A. P. Jauho, and M. Brandbyge, Thermoelectric properties of finite graphene antidot lattices, *Phys. Rev. B* 84(15), 155449 (2011)
29. H. Karamitaheri, M. Pourfath, R. Faez, and H. Kosina, Geometrical effects on the thermoelectric properties of ballistic graphene antidot lattices, *J. Appl. Phys.* 110(5), 054506 (2011)
30. Y. H. Yan, Q. F. Liang, H. Zhao, C. Q. Wu, and B. W. Li, Thermoelectric properties of one-dimensional graphene antidot arrays, *Phys. Lett. A* 376(35), 2425 (2012)

31. P.-H. Chang and B. K. Nikolić, Edge currents and nanopore arrays in zigzag and chiral graphene nanoribbons as a route toward high-ZT thermoelectrics, *Phys. Rev. B* 86(4), 041406(R) (2012)
32. M. Wierzbicki, R. Swirkowicz, and J. Barnaś, Giant spin thermoelectric efficiency in ferromagnetic graphene nanoribbons with antidots, *Phys. Rev. B* 88(23), 235434 (2013)
33. J. R. Williams, L. DiCarlo, and C. M. Marcus, Quantum hall effect in a gate-controlled p-n junction of graphene, *Science* 317(5838), 638 (2007)
34. T. Lohmann, K. von Klitzing, and J. H. Smet, Four terminal magneto-transport in graphene p-n junctions created by spatially selective doping, *Nano Lett.* 9(5), 1973 (2009)
35. L. DiCarlo, J. R. Williams, Y. M. Zhang, D. T. McClure, and C. M. Marcus, Shot noise in graphene, *Phys. Rev. Lett.* 100(15), 156801 (2008)
36. N. N. Klimov, S. T. Le, J. Yan, P.Agnihotri, E. Comfort, J. U. Lee, D. B. Newell, and C. A. Richter, Edge-state transport in graphene p-n junctions in the quantum Hall regime, *Phys. Rev. B* 92(24), 241301(R) (2015)
37. T. Ohta, A. Bostwick, T. Seyller, K. Horn, and E. Rotenberg, Controlling the electronic structure of bilayer graphene, *Science* 313(5789), 951 (2006)
38. E. D. Herbschleb, R. K. Puddy, P. Marconcini, J. P. Griffiths, G. A. C. Jones, M. Macucci, C. G. Smith, and M. R. Connolly, Direct imaging of coherent quantum transport in graphene p-n-p junctions, *Phys. Rev. B* 92(12), 125414 (2015)
39. B. Özyilmaz, P. Jarillo-Herrero, D. Efetov, D. A. Abanin, L. S. Levitov, and P. Kim, Electronic transport and quantum hall effect in bipolar graphene p-n-p junctions, *Phys. Rev. Lett.* 99(16), 166804 (2007)
40. R. N. Sajjad and A. W. Ghosh, High efficiency switching using graphene based electron optics, *Appl. Phys. Lett.* 99(12), 123101 (2011)
41. A. F. Young and P. Kim, Quantum interference and Klein tunnelling in graphene heterojunction, *Nat. Phys.* 5(3), 222 (2009)
42. C. H. Park, Y. W. Son, L. Yang, M. L. Cohen, and S. G. Louie, Electron beam supercollimation in graphene superlattices, *Nano Lett.* 8(9), 2920 (2008)
43. M. Woszczyna, M. Friedemann, T. Dziomba, T. Weimann, and F. J. Ahlers, Graphene p-n junction arrays as quantum-Hall resistance standards, *Appl. Phys. Lett.* 99(2), 022112 (2011)
44. T. Low and J. Appenzeller, Electronic transport properties of a tilted graphene p-n junction, *Phys. Rev. B* 80(15), 155406 (2009)
45. Y. X. Xing, J. Wang, and Q. F. Sun, Focusing of electron flow in a bipolar graphene ribbon with different chiralities, *Phys. Rev. B* 81(16), 165425 (2010)
46. N. Dai and Q. F. Sun, Mode mixing induced by disorder in a graphene pnp junction in a magnetic field, *Phys. Rev. B* 95(6), 064205 (2017)
47. H. Y. Tian, K. S. Chan, and J. Wang, Efficient spin injection in graphene using electron optics, *Phys. Rev. B* 86(24), 245413 (2012)
48. F. M. Xu, Z. Z. Yu, Z. R. Gong, and H. Jin, Firstprinciples study on the electronic and transport properties of periodically nitrogen-doped graphene and carbon nanotube superlattices, *Front. Phys.* 12(4), 127306 (2017)
49. B. H. Zhou, B. L. Zhou, Y. G. Yao, G. H. Zhou, and M. Hu, Spin-dependent Seebeck effects in a graphene superlattice p-n junction with different shapes, *J. Phys.: Condens. Matter* 29(40), 405303 (2017)
50. S. Datta, Quantum Transport-Atom to Transistor, England: Cambridge University Press, 2005
51. H. J. W. Haug and A.P. Jauho, Quantum Kinetics in Transport and Optics of Semiconductors, Berlin: Springer, 1998
52. A. P. Jauho, N. S. Wingreen, and Y. Meir, Timedependent transport in interacting and noninteracting resonanttunneling systems, *Phys. Rev. B* 50(8), 5528 (1994)
53. K. S. Novoselov, A. K. Geim, S. V. Morozov, D. Jiang, Y. Zhang, S. V. Dubonos, I. V. Grigorieva, and A. A. Firsov, Electric field effect in atomically thin carbon films, *Science* 306(5696), 666 (2004)
54. Y. B. Zhang, Y. W. Tan, H. L. Stormer, and P. Kim, Experimental observation of the quantum Hall effect and Berry's phase in graphene, *Nature* 438(7065), 201 (2005)
55. L. Ci, L. Song, D. Jariwala, A. L. ElÃas, W. Gao, M. Terrones, and P. M. Ajayan, Graphene shape control by multistage cutting and transfer, *Adv. Mater.* 21(44), 4487 (2009)
56. H. Haugen, D. Huertas-Hernando, and A. Brataas, Spin transport in proximity-induced ferromagnetic graphene, *Phys. Rev. B* 77(11), 115406 (2008)
57. K. H. Ding, Z. G. Zhu, and G. Su, Spin-dependent transport and current-induced spin transfer torque in a strained graphene spin valve, *Phys. Rev. B* 89(19), 195443 (2014)
58. Q. F. Sun and X. C. Xie, CT-invariant quantum spin hall effect in ferromagnetic graphene, *Phys. Rev. Lett.* 104(6), 066805 (2010)
59. M. P. L. Sancho, J. M. L. Sancho, J. M. L. Sancho, and J. Rubio, Highly convergent schemes for the calculation of bulk and surface Green functions, *J. Phys. F Met. Phys.* 15(4), 851 (1985)
60. D. H. Lee and J. D. Joannopoulos, Simple scheme for surfaceband calculations (II): The Green's function, *Phys. Rev. B* 23(10), 4997 (1981)
61. R. Świrkowicz, M. Wierzbicki, and J. Barnaś, Thermoelectric effects in transport through quantum dots attached to ferromagnetic leads with noncollinear magnetic moments, *Phys. Rev. B* 80(19), 195409 (2009)

62. P. Trocha and J. Barnaś, Large enhancement of thermoelectric effects in a double quantum dot system due to interference and Coulomb correlation phenomena, *Phys. Rev. B* 85(8), 085408 (2012)

63. X. B. Chen, D. P. Liu, W. H. Duan, and H. Guo, Photon-assisted thermoelectric properties of non-collinear spin valves, *Phys. Rev. B* 87(8), 085427 (2013)

64. S. H. Lv, S. B. Feng, and Y. X. Li, Thermopower and conductance for a graphene p-n junction, *J. Phys. Condens. Matter* 24(14), 145801 (2012)

65. T. Rejec, A. Ramšak, and J. H. Jefferson, Spin-dependent thermoelectric transport coe_cients in near perfect quantum wires, *Phys. Rev. B* 65(23), 235301 (2002)

66. B. H. Zhou, B. L. Zhou, Y. S. Zeng, G. H. Zhou, and T. Ouyang, Seebeck effects in a graphene nanoribbon coupled to two ferromagnetic leads, *J. Appl. Phys.* 115(11), 114305 (2014)
B. H. Zhou, B. L. Zhou, Y. S. Zeng, G. H. Zhou, and T. Ouyang, Spin-dependent Seebeck effects in a graphene nanoribbon coupled to two square lattice ferromagnetic leads, *J. Appl. Phys.* 117(10), 104305 (2015)

67. L. J. Yin, K. K. Bai, W. X. Wang, S. Y. Li, Y. Zhang, and L. He, Landau quantization of Dirac fermions in graphene and its multilayers, *Front. Phys.* 12(4), 127208 (2017)